Available online at www.sciencedirect.com
ScienceDirect
International Journal of Heat and Mass Transfer 51 (2008) 4659–4675
International Journal of HEAT and MASS TRANSFER
www.elsevier.com/locate/ijhmt

Assessment of performance of turbulence models in predicting supercritical pressure heat transfer in a vertical tube

S. He [a,*], W.S. Kim [a], J.H. Bae [b]

[a] School of Engineering, University of Aberdeen, Aberdeen AB24 3UE, UK
[b] School of Mechanical and Aerospace Engineering, Seoul National University, Seoul 151-744, Korea

Received 26 November 2007
Available online 9 May 2008

Abstract

Computational simulations of heat transfer to fluids at a supercritical pressure have been performed using an 'in-house' CFD code written for two-dimensional axisymmetric flow and heat transfer based on the Favre averaging approach. Results are compared with recently available direct numerical simulations (DNS) which provide a benchmark dataset ideal for model assessment. The objective of the present study is to evaluate the performance of low-Reynolds number turbulence models in predicting mixed convection heat transfer to fluids at supercritical pressure, especially paying attention to the features which enable them to respond to the modifications of the turbulence field due to influences of flow acceleration and buoyancy. It has been found that a group of turbulence models which were previously found closely reproducing mixed convection under conditions of constant properties do not perform well for flows considered in the present study due to an over-response to changes in the flow. Models which were less successful previously perform better. The V2F model performs the best among all models tested. For strong-buoyancy-influenced cases, most models are able to reproduce turbulence recovery reasonably well but not the improvement on heat transfer. This is attributed, at least partly, to the inability of turbulence models in reproducing turbulent heat flux using a constant turbulent Prandtl number. The influence of the lack of a suitable description of the axial turbulent heat flux has been shown to be insignificant except immediately after the commencement of heating.

Keywords: Supercritical pressure; Mixed convection; Buoyancy; Acceleration; Heat transfer deterioration

1. Introduction

A fluid remains the same phase regardless of its temperature when the pressure of the fluid is above the thermal critical value, i.e., at a *supercritical pressure*. However, the properties of the fluid can vary rapidly with both pressure and temperature. In particular, the specific heat capacity exhibits a sharp peak at a temperature known as pseudo-critical temperature, T_{pc}. Other properties such as density, viscosity and thermal conductivity also vary significantly within a small temperature window in the vicinity of T_{pc}. In convective heat transfer applications involving fluids near the critical condition, the diffusion of heat (by both molecular and turbulent action) can be strongly affected by these variations of properties. Especially the variations of density can affect turbulence production, either by virtue of the flow *acceleration* due to thermal expansion of the heated fluid or because of the influences of *buoyancy*. These effects combined with large variations of specific heat and thermal conductivity may have very important consequences in terms of effectiveness of heat transfer.

Extensive studies on supercritical pressure heat transfer were conducted in the 1960's and 1970's in support of the development of conventional supercritical water power stations but much less studies have been conducted since then. Recently there has been a renewed interest in the subject driven by active considerations in Europe, Japan, Canada and America in the development of the Supercritical Water-Cooled Nuclear Reactors (SCWR's) [1,2] and several other

* Corresponding author. Tel.: +44 1224 272799; fax: +44 1224 272497.
E-mail address: s.he@abdn.ac.uk (S. He).

0017-9310/$ - see front matter © 2008 Elsevier Ltd. All rights reserved.
doi:10.1016/j.ijheatmasstransfer.2007.12.028

Nomenclature

Bo^*	buoyancy parameter, $[= Gr^*/(Re^{3.425}Pr^{0.8})]$
c_p	specific capacity at constant pressure
$C_{\varepsilon 1}$, $C_{\varepsilon 2}$	constants in the ε-equation
C_μ	constant in constitutive equation of eddy viscosity model
D	additional term in the k-equation or diameter
E	additional term in the ε-equation
f	elliptic relation parameter
f_1, f_2	functions in dissipation equation
f_μ	damping function in the constitutive equation
g	acceleration due to gravity
G_k	buoyant production
Gr^*	Grashof number, $Gr^* = \beta g D^4 q_w/(\lambda \nu^2)$
h	heat transfer coefficient, $q_w/(T_w - T_b)$; *enthalpy*
k	turbulent kinetic energy
Nu	Nusselt number,
Nu_f	Nusselt number for forced convection
p	pressure
P_k	turbulent shear production
Pr	Prandtl number, $Pr = \mu c_p/\lambda$
q_w	convective heat flux from the wall
r	radial coordinate
R	Radius of pipe
Re	Reynolds number, $Re = u_b D/\nu$
$\overline{t^2}$	temperature variance
T	temperature
T_t	turbulence time scale $(= k/\varepsilon)$
u, v	velocity components in x, r-directions
uv	turbulent shear stress
v^2	variance of the normal component of turbulent velocity
x	axial coordinate
y	distance from pipe wall in the direction normal to it
y^+	non-dimensional distance from pipe wall, $\rho_w y(\tau_w/\rho_w)^{1/2}/\mu_w$

Greek symbols

β	thermal expansion coefficient
ε	dissipation rate of k
ε_t	dissipation rate of
λ	thermal conductivity
μ	molecular viscosity
μ_t	turbulent viscosity
ν	kinematic viscosity, $\nu = \mu/\rho$
τ_w	wall shear stress
ρ	density
σ_k, σ_ε, σ_T	turbulent Prandtl number for k, ε and T

Subscripts/over-bars

0	inlet
b	bulk
cp	constant property
f	forced
pc	pseudo-critical
w	wall
'–'	over-bar used for conventional average
'∼'	over-bar used for Faver average

new applications involving supercritical pressure fluids. For example, supercritical pressure water oxidation (SCWO) has emerged in recent years as a promising technology for the de-structuring of toxic organic materials [3]. Carbon dioxide operating at transcritical conditions has recently been subjected to scrutiny as a refrigerant to replace CFCs and HCFCs air conditioning equipment in order to reduce the damage to the ozone layer [4,5]. There is also an interest in using supercritical pressure hydrogen in the active cooling of a reusable Earth-to-orbit hypersonic aircraft [6].

Comprehensive reviews of earlier experimental studies on heat transfer to water and carbon dioxide at supercritical pressure were provided in two review papers [7,8]. More recent studies include experiments carried out by Pitla et al. [5] and Dang and Hihara [9] under conditions of cooling of CO_2 flowing in vertical tubes and Liao and Zhao [10,11] and Jiang et al. [12] in mini/micro tube of diameters less than 1 mm. In addition, measurements of wall temperature were performed by Kim et al. [13] for several non-circular channels including rectangular and triangular passages.

Considerable attention has also been devoted to modelling of flow and heat transfer involving fluids at supercritical pressure using computational fluid dynamics (CFD). Youn and Mills [6] and Dang and Hihara [14] studied heat transfer to supercritical pressure hydrogen and carbon dioxide, respectively, under *forced* convection condition using low-Reynolds number turbulence models. Because buoyancy was considered insignificant and excluded in the simulations, the main influences were from the non-uniformity of fluid properties and possibly thermally induced flow acceleration. The turbulence models used were found to be able to reproduce the experiments fairly well under many conditions though there were big variations between the performances of the various models.

Koshizuka et al. [15] and He et al. [16,17] conducted numerical simulations of *mixed* convection to water and carbon dioxide at supercritical pressure in vertical tubes. Between the studies, a number of low-Reynolds number turbulence models have been examined and predictions compared with experiments under a wide range of conditions. Overall it has been found that most low-Reynolds number turbulence models examined can reproduce the *trend* of flow laminarization and heat transfer deterioration under the influence of buoyancy, although some models can do much better than others in terms of quantitative comparison with experimental data.

Lee and Howell [18] and Asinari [19] argued that density fluctuations in supercritical pressure flow can be very strong and make a significant contribution to momentum and heat transfer. They have therefore retained terms such as $\overline{\rho' u'}$ and $\overline{\rho' v'}$ in the formulation of their simulations and developed models for them. Improvements over conventional models have been found. Pitla et al. [4] adopted a different approach to tackle issues related to density fluctuations. He used the Favre averaging approach instead of the conventional Reynolds average but a rather basic one-equation turbulence model developed for incompressible flow was used to account for turbulence mixing.

More recently, commercial CFD packages have been employed in simulations of supercritical pressure flow by several groups, including Sharabi et al. [20] using Fluent, Yang et al. [21] using Star-CD and Cheng et al. [22] using CFX. A range of turbulence models embedded in the packages, including both low-Reynolds number and wall-function turbulence models, have been examined. Rather encouraging results have been obtained in terms of reproducing the general trends exhibited by the experimental data. Simulations of non-circular channels, including subchannels of fuel bundles in nuclear reactors, have also been attempted by all of these studies and useful results have been obtained.

It has become clear from the recent computational studies reviewed above that, over quite a range of conditions, suitably selected turbulence models can reproduce the general *trend* of heat transfer enhancement and deterioration exhibited by experiments of supercritical pressure flows, but detailed comparison with experiments and the consistency of performance can vary significantly from model to model and for the same model, from condition to condition. The low-Reynolds number feature of turbulence models which enable them to respond to local flow distortions is clearly very important to enable the model to reproduce the influences of buoyancy and effects due to large variations of fluid properties. Due to technical difficulties associated with heated supercritical pressure flows, the majority of experiments provide only heat transfer data. Very little have been done in obtaining detailed information on the flow and turbulence for supercritical pressure flow. This has made it difficult to understand why turbulence models perform the way they do and to improve their performance and develop better models.

Recently, Bae et al. [23] have conducted direct numerical simulations (DNS) of carbon dioxide at a supercritical pressure flowing in a vertical tube subjected to heating from the wall. The study has produced detailed information on the flow, turbulence and thermal fields which is extremely difficult to obtain from physical experiments, hence providing a good opportunity for a detailed assessment of the performance of turbulence models. Simulations of the DNS data using a number of low-Reynolds number turbulence models have been carried out by the present authors which are presented in the present paper. The objective is to evaluate the performance of the turbulence models through detailed comparisons with the DNS data, paying attention to the features which enable them to respond to the modifications of the turbulence field due to influences of non-uniformity of fluid property and buoyancy.

2. Methodology

2.1. Brief description of the DNS of Bae et al. [23]

The governing equations solved in the DNS were based on the full 3D Navier Stokes equations with the low-Mach-number assumption with which the acoustic interactions and compressibility effects were eliminated. Under such conditions, the thermodynamic state variables such as density and enthalpy are independent of the fluctuations of pressure which significantly reduced numerical difficulties associated with the limitations on the maximum time steps that could be used. The continuity, momentum and enthalpy equations written in cylindrical coordinates in a non-dimensional form were discretized using a conservative space-time scheme in which the velocity was staggered by one-half grid spatially and one-half temporally with respect to density and other scalar variables. The density and other thermodynamic properties of CO_2 were calculated using the computer program PROPATH [24]. A fully developed flow of carbon dioxide which had been generated using an inlet flow generator entered the vertical tube from either the top or bottom (dependent on whether an up or downward flow was simulated) of the tube which was heated uniformly from the wall. The inlet conditions are $P_0 = 8$ MPa, $T_0 = 301.15$ K, $Re_0 = 5400$ and $Pr_0 = 3.08$. Simulations for forced and mixed convection for both up and downward flows were carried out for flows under a range of conditions with increasing effects of buoyancy or thermally induced acceleration. In the present study, we have chosen a series of cases with increasing values of buoyancy parameter but a fixed normalised heat flux. Consequently, the acceleration effect can be considered the same in all cases. Studies are focused on upward flow only. The conditions of DNS cases which have been simulated in this study are summarised in Table 1.

The DNS code was validated using the experimental data of Shehata and McEligot [25] for strongly heated internal gas flows with large variations of gas properties due to heat transfer. The predictions of the overall heat

Table 1
Conditions of simulations

Case	Type	Dir.	D (mm)	q_w (kW/m^2)	$Bo^* \times 10^5$
A	Forced	Up	1.0	61.74	0
B	Mixed	Up	1.0	61.74	0.141
C	Mixed	Up	2.0	30.87	1.124
D	Mixed	Up	3.0	20.58	3.794

Notes: (1) $P = 8$ MPa, $T_{in} = 28$ °C, $Re_{in} = 5400$.
(2) Buoyancy parameter, $Bo^* = Gr/(Re^{3.425}Pr^{0.8})$.

transfer parameter, as well as the mean velocity and temperature distributions were found to be in excellent agreement with experimental data. Direct comparisons were shown in the DNS paper [23]. Efforts have been also made to compare DNS results with experiments of heat transfer to supercritical pressure carbon dioxide of Fewster and Jackson [33] based on ratios of Nusselt numbers (Nu/Nu_f), where Nu is the local Nusselt number of mixed convection and Nu_f is that of forced convection. Excellent agreement was achieved for both up and downward flows, although the Reynolds number of the DNS was much lower than that in the experiment.

2.2. Governing equations and turbulence modelling

The governing equations solved in the present study are the Favre averaged form of the continuity, momentum and enthalpy equations used in the DNS [23]. The Favre averaging approach enables the strong fluctuations of density under conditions of supercritical pressure to be simulated while retaining the relatively simple form of the equations obtained through the conventional Reynolds averaging approach for incompressible flows. Unlike the DNS, the flow is assumed to be 2D axisymmetric in the present study and the governing equations for such a flow written in cylindrical coordinates read:

Continuity

$$\frac{1}{r}\left\{\frac{\partial}{\partial x}(r\bar{\rho}\tilde{u})+\frac{\partial}{\partial r}(r\bar{\rho}\tilde{v})\right\}=0 \tag{1}$$

U-momentum

$$\begin{aligned}\frac{1}{r}&\left\{\frac{\partial}{\partial x}(r\bar{\rho}\tilde{u}^2)+\frac{\partial}{\partial r}(r\bar{\rho}\tilde{v}\tilde{u})\right\}\\&=-\frac{\partial\bar{p}}{\partial x}+\bar{\rho}g+\frac{1}{r}\left\{2\frac{\partial}{\partial x}\left[r\mu_e\left(\frac{\partial\tilde{u}}{\partial x}\right)\right]\right.\\&\left.+\frac{\partial}{\partial r}\left[r\mu_e\left(\frac{\partial\tilde{u}}{\partial r}+\frac{\partial\tilde{v}}{\partial x}\right)\right]\right\}\end{aligned} \tag{2}$$

V-momentum

$$\begin{aligned}\frac{1}{r}&\left\{\frac{\partial}{\partial x}(r\bar{\rho}\tilde{u}\tilde{v})+\frac{\partial}{\partial r}(r\bar{\rho}\tilde{v}^2)\right\}=-\frac{\partial\bar{p}}{\partial r}+\frac{1}{r}\left\{\frac{\partial}{\partial x}\left[r\mu_e\left(\frac{\partial\tilde{v}}{\partial x}+\frac{\partial\tilde{u}}{\partial r}\right)\right]\right.\\&\left.+2\frac{\partial}{\partial r}\left[r\mu_e\left(\frac{\partial\tilde{v}}{\partial r}\right)\right]\right\}-2\frac{\mu_e\tilde{v}}{r^2}\end{aligned} \tag{3}$$

in which μ_e is the effective viscosity defined by $\mu_e=\bar{\mu}+\bar{\mu}_t$ and $\bar{\mu}_t$ is the turbulent viscosity, which is defined as

$$\bar{\mu}_t=\bar{\rho}C_\mu f_\mu\frac{\tilde{k}^2}{\tilde{\varepsilon}} \tag{4}$$

in which f_μ is a damping function to account for near-wall effects and C_μ is a constant.

Energy

$$\begin{aligned}\frac{1}{r}&\left\{\frac{\partial}{\partial x}(r\bar{\rho}\tilde{u}\tilde{h})+\frac{\partial}{\partial r}(r\bar{\rho}\tilde{v}\tilde{h})\right\}\\&=\frac{1}{r}\left\{\frac{\partial}{\partial x}\left[r\left(\frac{\bar{\mu}}{\overline{Pr}}+\frac{\bar{\mu}_T}{\sigma_T}\right)\frac{\partial\tilde{h}}{\partial x}\right]+\frac{\partial}{\partial r}\left[r\left(\frac{\bar{\mu}}{\overline{Pr}}+\frac{\bar{\mu}_T}{\sigma_T}\right)\frac{\partial\tilde{h}}{\partial r}\right]\right\}\end{aligned} \tag{5}$$

in which $\overline{Pr}$ is the molecular Prandtl number and σ_T is the turbulent Prandtl number. The over-bar '–' and tilde '∼' represent conventional time averaging and Favre averaging, respectively.

Turbulence models which have been developed for incompressible flows are used by re-writing them in the Favre averaging form. No special adjustment has been made to the models. We are particularly concerned with '*low-Reynolds number*' eddy viscosity turbulence models since that feature has been found in earlier studies to be essential to simulate '*non-equilibrium*' flows such as these under consideration here as mentioned earlier. We aim to cover a broad spectrum of such models but with some emphasis on those which were developed targeting at improving mixed convection heat transfer. With this in mind we have selected some '*classical*' k–ε models: Launder and Sharma (LS) [26], Chien (CH) [27], a k–ω model by Wilcox (WI) [28], and some more recent models: Myoung and Kasagi (MK) [29], Yang and Shih (YS) [30] and Abe, Kondoh and Nagano (AKN) [31]. The k–ε–v^2–f model of Behnia, Parneix and Durbin (V2F) [32] has also been included since this model has been found to perform better than many k–ε models in some recent studies of variable property heat transfer.

The general form of k–ε models can be expressed as follows with constants and damping functions defined in Appendix 1:

Turbulent kinetic energy

$$\begin{aligned}\left[\frac{\partial(\bar{\rho}\tilde{u}\tilde{k})}{\partial x}+\frac{1}{r}\frac{\partial(r\bar{\rho}\tilde{v}\tilde{k})}{\partial r}\right]&=\frac{\partial}{\partial x}\left[\left(\bar{\mu}+\frac{\bar{\mu}_t}{\sigma_k}\right)\frac{\partial\tilde{k}}{\partial x}\right]\\&+\frac{1}{r}\frac{\partial}{\partial r}\left[r\left(\bar{\mu}+\frac{\bar{\mu}_t}{\sigma_k}\right)\frac{\partial\tilde{k}}{\partial r}\right]\\&+P_k+G_k-\bar{\rho}(\tilde{\varepsilon}-D)\end{aligned} \tag{6}$$

in which

$$P_k=\bar{\mu}_t\left[2\left\{\left(\frac{\partial\tilde{u}}{\partial x}\right)^2+\left(\frac{\partial\tilde{v}}{\partial r}\right)^2+\left(\frac{\tilde{v}}{r}\right)^2\right\}+\left(\frac{\partial\tilde{u}}{\partial r}+\frac{\partial\tilde{v}}{\partial x}\right)^2\right]$$

(shear production)

and

$$\begin{aligned}G_k&=-\overline{\rho' u'}g_x\\&=-c_\theta\beta\bar{\rho}g_x\frac{\tilde{k}}{\tilde{\varepsilon}}\left[\mu_t\left(\frac{\partial\tilde{u}}{\partial r}+\frac{\partial\tilde{v}}{\partial x}\right)\frac{\partial\widetilde{T}}{\partial r}+\left(2\bar{\mu}_t\frac{\partial\tilde{u}}{\partial x}-\frac{2}{3}\bar{\rho}\tilde{k}\right)\frac{\partial\widetilde{T}}{\partial x}\right]\end{aligned}$$

(gravitational production)

where $g_x = -g$ for upward flow, $g_x = g$ for downward flow and $c_\theta = 0.3$.

Turbulence dissipation rate

$$\left[\frac{\partial(\bar{\rho}\tilde{u}\tilde{\varepsilon})}{\partial x}+\frac{1}{r}\frac{\partial(r\bar{\rho}\tilde{v}\tilde{\varepsilon})}{\partial r}\right]=\frac{\partial}{\partial x}\left[(\bar{\mu}+\frac{\bar{\mu}_t}{\sigma_\varepsilon})\frac{\partial\tilde{\varepsilon}}{\partial x}\right]+\frac{1}{r}\frac{\partial}{\partial r}\left[r(\bar{\mu}+\frac{\bar{\mu}_t}{\sigma_\varepsilon})\frac{\partial\tilde{\varepsilon}}{\partial r}\right]+C_{\varepsilon 1}f_1\frac{1}{T_t}P_k+C_{\varepsilon 1}f_1\frac{1}{T_t}G_k-C_{\varepsilon 2}f_2\frac{\bar{\rho}\tilde{\varepsilon}}{T_t}+\bar{\rho}E,\quad \text{where, } T_t=\tilde{k}/\tilde{\varepsilon} \tag{7}$$

The V2F model [32] has two additional equations (for $\widetilde{v^2}$ and $\tilde{f}$) and additional parameters as shown below:

Turbulent velocity scale $(\widetilde{v^2})$

$$\left[\frac{\partial(\bar{\rho}\tilde{u}\widetilde{v^2})}{\partial x}+\frac{1}{r}\frac{\partial(r\bar{\rho}\tilde{v}\widetilde{v^2})}{\partial r}\right]=\frac{\partial}{\partial x}\left[\left(\bar{\mu}+\frac{\bar{\mu}_t}{\sigma_k}\right)\frac{\partial\widetilde{v^2}}{\partial x}\right]+\frac{1}{r}\frac{\partial}{\partial r}\left[r\left(\bar{\mu}+\frac{\bar{\mu}_t}{\sigma_k}\right)\frac{\partial\widetilde{v^2}}{\partial r}\right]+\tilde{k}\tilde{f}-6\widetilde{v^2}\frac{\tilde{\varepsilon}}{\tilde{k}} \tag{8}$$

Production $(\tilde{f})$

$$0=\frac{\partial}{\partial x}\left(\frac{\partial\tilde{f}}{\partial x}\right)+\frac{1}{r}\frac{\partial}{\partial r}\left(r\frac{\partial\tilde{f}}{\partial r}\right)-\frac{1}{L^2}\tilde{f}+\frac{(C_1-1)}{L^2}\times\frac{(2/3-\widetilde{v^2}/\tilde{k})}{T_t}+\frac{C_2}{L^2}\frac{1}{\bar{\rho}\tilde{k}}(P_k)+\frac{1}{L^2}\frac{5\widetilde{v^2}/\tilde{k}}{T_t} \tag{9}$$

Here, the turbulent viscosity is defined as follows:

$$\bar{\mu}_t=\bar{\rho}C_\mu\widetilde{v^2}T_t \tag{10}$$

where $T_t=\max\left[\frac{\tilde{k}}{\tilde{\varepsilon}},6\sqrt{\frac{\bar{\mu}}{\bar{\rho}\tilde{\varepsilon}}}\right]$, $L=C_L\max\left[\frac{\tilde{k}^{3/2}}{\tilde{\varepsilon}},C_\eta\left(\frac{(\bar{\mu}/\bar{\rho})^3}{\tilde{\varepsilon}}\right)^{1/4}\right]$,

$C_1 = 1.4$, $C_2 = 0.3$, $C_\eta = 70$, $C_\mu = 0.22$, $C_L = 0.23$. Conceptually, Eq. (10) can be re-written in the form of Eq. (5) with the damping function f_μ defined as:

$$f_\mu=\widetilde{v^2}T_t/(\tilde{k}^2/\tilde{\varepsilon}). \tag{11}$$

2.3. Numerical method

The current computational study has been conducted using an 'in-house' CFD code named SWIRL based on the widely used finite volume scheme. The staggered grid arrangement was used to define the variables. The QUICK scheme was used for approximating the convection terms in the momentum equations and the UPWIND scheme was used for other transport equations for reasons of numerical stability which is an important issue when supercritical fluid is considered. The SIMPLE scheme was used for coupling the pressure and the velocity fields. The resultant five-point coefficient matrix system was solved iteratively using the line-by-line TDMA algorithm. To be consistent with the DNS, the pressure and temperature dependent properties of carbon dioxide were calculated using the program PROPATH [24]. The complete computational domain, which covered the whole heated length of the test section and around 40 diameter length of the preheated section and ranged from the centre of the tube to the inner wall, was discretized into a mesh of grids, typically, 120 × 106 (axial × radial). The mesh was refined in the radial direction towards the tube wall. It was also refined in the axial direction towards the region where the heating commenced. The mesh was adjusted in each individual run to ensure that the near-wall flow features were properly resolved and the y^+ value at the first node of the mesh was always less than 0.5. The computer code SWIRL was previously used and validated in several earlier studies of convective heat transfer. These include modelling of experiments of Jiang et al. [12] for mini/micro-channels in which excellent agreement between experiments and simulations was achieved [17] and modelling of experiments of Fewster and Jackson [33] which were carried out at a pressure *just above* the critical value [34]. Turbulence models used in the latter study were not able to reproduce the dramatic changes in the variations of wall temperatures exhibited by the experimental data which resulted from the very strong variations of thermal properties with temperature of the fluid at a pressure close to the critical value. However the general trend was well captured.

3. Results and discussion

3.1. Prediction of wall temperature

Fig. 1 shows the development of the wall temperature in several cases predicted by various turbulence models together with those obtained from the DNS. It is clear that, the LS, YS and AKN models consistently over-predict the wall temperature for each of the cases. The CH and MK models reproduce the DNS wall temperature fairly well for cases A and B, but over-predict it for cases C and D although to a lesser extent than the first group of models do. The V2F model appears to produce the best prediction of wall temperature among all the models tested whereas the performance of the WI is similar to that of the second group of the models. In an early study reported in Kim et al. [35], turbulence models were categorized into two groups, i.e., those whose damping functions respond rather strongly to changes in local flow conditions (Group I model), and those whose damping function do not (or only weakly) respond to local flow conditions (Group II). Examples of damping functions used in Group I models are those based on $Re_t = k^2/\varepsilon\upsilon$ and those used in Group II are those based on y^+. The LS, YS and AKN models were then identified as Group I models and CH and MK Group II models in that study. It is of interest to note that models from the same group again perform in a similar manner in the current simulations as seen above.

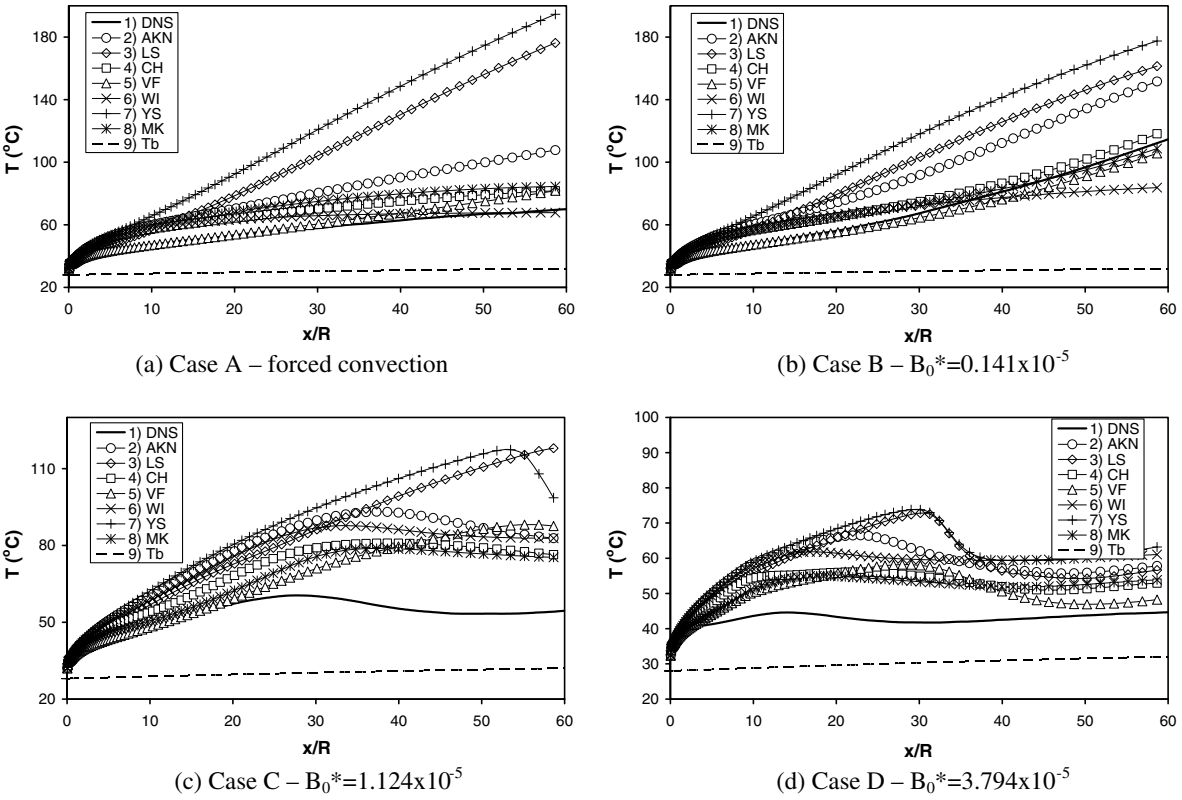

(a) Case A – forced convection

(b) Case B – B_0*=0.141x10^{-5}

(c) Case C – B_0*=1.124x10^{-5}

(d) Case D – B_0*=3.794x10^{-5}

Fig. 1. Development of wall and bulk temperatures along the pipe.

The effects of buoyancy and flow acceleration on heat transfer can be better studied by considering the ratio of the Nusselt number in the mixed convection flow to that in a flow under corresponding conditions but with the influences of buoyancy and flow acceleration absent. Nusselt numbers for the latter can be calculated using semi-empirical correlations for forced convection heat transfer without corrections accounting for buoyancy or acceleration. Such Nusselt number ratios calculated from the results of simulations using the various turbulence models and those from the DNS data for the location at $x/R = 60$ are shown in Fig. 2. The reference Nusselt number Nu_f is calculated using the modified Krasnoshchekov and Protopopov correlation (see [23]):

$$Nu_f = 0.0183 Re_b^{0.82} Pr_b^{0.4} \left(\frac{\rho_w}{\rho_b}\right)^{0.3} \left(\frac{\overline{c_p}}{c_{pb}}\right)^n \tag{12}$$

where $\bar{c}_p = \frac{1}{T_w - T_b} \int_{T_b}^{T_w} c_p dT = \frac{h_w - h_b}{T_w - T_b}$ and the exponent n is obtained from

$$n = \begin{cases} 0.4 \quad \text{for } T_b < T_w \leqslant T_{pc} \text{ or } 1.2T_{pc} \leqslant T_b < T_w, \\ 0.4 + 0.2(T_w/T_{pc} - 1) \quad \text{for } T_b \leqslant T_{pc} < T_w, \\ 0.4 + 0.2(T_w/T_{pc} - 1)[1 - 5(T_b/T_{pc} - 1)] \quad \text{for } T_{pc} < T_b \leqslant 1.2T_{pc} \quad \text{and} \quad T_b < T_w \end{cases} \tag{13}$$

First consider Case A, in which the buoyancy term in the momentum equation has been removed, hence noted as forced convection. Under such a condition, heat transfer deterioration that exhibits in the results (e.g., the Nusselt number ratio being smaller than unity) is caused purely by thermally induced flow acceleration. The DNS data show a 20% reduction in Nu, which has been well reproduced by Group II models as well as by the V2F and WI models. Group I models predict much larger reductions in Nu. Case B represents a condition where the flow is largely laminarized and severe heat transfer deterioration occurs due to the combined influence of buoyancy and flow acceleration. Again, Group II models and the V2F reproduce the DNS data closely but WI in this case under-predicts heat transfer deterioration. Group I models again over-predict heat transfer deterioration. Cases C and D represent a condition in which buoyancy is so strong that the velocity profile is inverted to an M-shape with the maximum velocity moving away from the centre to a location close to the wall. Mixed convection under such a condition is said to have reached the recovery regime since turbulence begins to be regenerated in the core due to the inverted velocity profile, leading to heat transfer improvement. In

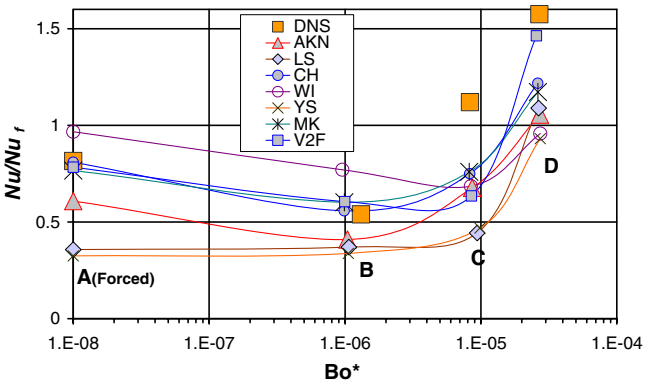

Fig. 2. Nusselt number ratios.

fact, heat transfer can even be more effective than in forced convection, which is represented by a *Nu* ratio greater than unity. It is clear that under these conditions, all models significantly under-predict heat transfer recovery except in Case D where V2F appears to predict a *Nu* ratio close to the DNS value.

The above observations on the performance of Groups I and II models compare interestingly with the results of Kim et al. [35] mentioned above in which the performance of turbulence models for the prediction of mixed convection were assessed for conditions at which fluid properties were taken to be constant and buoyancy was accounted for using the Boussinesq approach. It was then found that Group I and V2F models performed generally well in predicting heat transfer deterioration due to buoyancy whereas Group II models often responded too slow and too weak to the effect of buoyancy and consequently predicted lower wall temperatures than those obtained from DNS under the same conditions. The performance of the models was associated with the ability of the damping functions of the respective group of models responding to local flow conditions. Although models from the same group again perform in a similar manner in the current study, Group II models now appear to perform better than Group I models, the reasons of which will be discussed in the following section.

In the following sections, discussion will be based on results from two representative models, namely, the LS and the V2F models. The former represents Group I models where the latter, although not exactly a Group II model itself, often behaves in a very similar manner as a Group II model does in the current application. General conclusions will be drawn regarding other models wherever appropriate.

3.2. Velocity and turbulence fields

Figs. 3–5 show comparisons between the predictions of the LS and V2F models and the DNS of profiles of (a) the mean velocity, (b) turbulent kinetic energy and (c) turbulent shear stress at several locations along the heated pipe for cases A, B and D, respectively.

3.2.1. Forced convection (Case A)

The DNS results show that the velocity profile is flattened soon after the beginning of the heating under the influences of flow acceleration due to expansion of fluid with increasing temperature which is particularly strong near the pseudo-critical temperature. The overall level of turbulence quantities ($\tilde{k}$ and $\widetilde{uv}$) tends to reduce as the flow proceeds downstream, although near the wall ($y^+ < 10$), the normalised turbulent kinetic energy actually increases exhibiting a trend opposite to those commonly found in accelerating flows. This rather 'abnormal' effect is likely to be associated with the very non-uniform distribution of the local acceleration resulting from the characteristic variations of properties of fluid near the pseudo-critical temperature.

In response to the thermally induced flow acceleration, the LS model predicts successively reducing turbulence along the heated tube at a fashion significantly stronger than that exhibited by the DNS data. It is particularly noticeable that the turbulence (both $\tilde{k}$ and $\widetilde{uv}$) reduces very fast near the wall and nearly completely diminishes towards the end of the pipe showing a trend opposite to that exhibited by DNS. As a result, the effectiveness of heat transfer predicted by this model is much worsened leading to a wall temperature significantly higher than that of the DNS as seen earlier in Fig. 1.

The V2F model predictions follow fairly closely the DNS data with turbulence gradually reducing as flow proceeding downstream. The turbulence retains a fairly high level near the wall towards the later stages of the flow though the peaking in this region exhibited by the DNS results is not seen. The latter is likely to be responsible for the small but clear deviation of the wall temperature of the V2F model from that of the DNS shown in Fig. 1.

3.2.2. Laminarization of flow due to influence of buoyancy (Case B)

The basic flow condition in Case B is the same as in Case A except that the buoyant force is now included in the governing equations solved in the simulations. In a heated upward flow, buoyancy has an effect of increasing the velocity gradient very close to the wall and flattening it further out. This adds onto the effect of acceleration causing turbulence to reduce even further resulting in more severe flow laminarization as shown in the DNS results, although turbulent kinetic energy still exhibits a peak near the wall.

The LS model again predicts a faster and stronger flow laminarization than that exhibits by the DNS (Fig. 4). This is particularly true near the wall ($y^+ < 20$) where the LS model predicts turbulence diminishing completely. In fact, under the combined action of the acceleration and buoyancy, the flow predicted by the LS model begins to show signs of flow recovery after past through the worst flow laminarization, that is, the mean velocity begins to show an M-shaped profile and a small negative shear stress is produced. Consequently heat transfer begins to improve slightly and the wall temperature predicted by this model

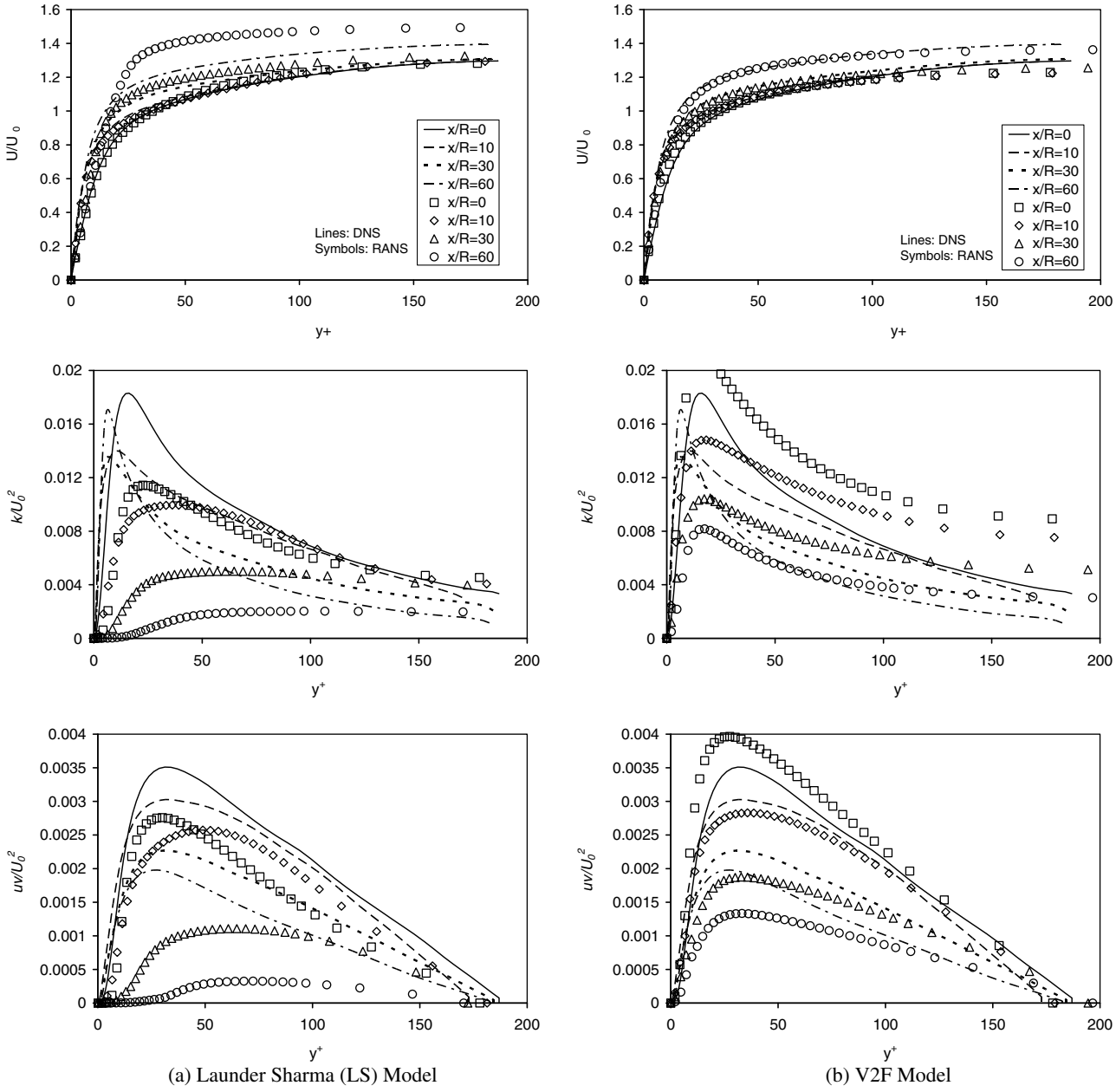

(a) Launder Sharma (LS) Model (b) V2F Model

Fig. 3. Forced convection with the influence of thermally induced flow acceleration (Case A).

increases slower in Case B than in Case A towards the later stages of the flow.

The prediction of the V2F model follows very closely the DNS data over the entire length of the heated pipe with the reduction of the turbulence as well as the mean velocity profiles closely reproduced. The only exception is again the peaking of turbulence near the wall exhibited by DNS not being reproduced. Nevertheless the variation of the wall temperature was well reproduced as discussed earlier (Fig. 1).

The wall temperature predicted by other models is also consistent with the turbulence predicted by them. For Group II models (including CH and MK) turbulence predicted shows a trend generally similar to that of the V2F model although a slight over-prediction of the reduction of turbulence in response to the influence of buoyancy is observed. All Group I models (such as YS and AKN) on the other hand significantly over-predict turbulence reduction, closely following the trend exhibited by the LS model.

To understand the reasons for the different performances of the various turbulence models, the radial profiles of the damping function f_μ at the various stages of the flow are shown in Fig. 6. Values of f_μ were calculated using Eq. (4) for the LS model and DNS, and Eq. (11) for the V2F model. The DNS result shows that the damping function actually increases over the first half length of the pipe, only reducing slightly towards the end of the heated flow in the near-wall region, although the overall turbulence deceases

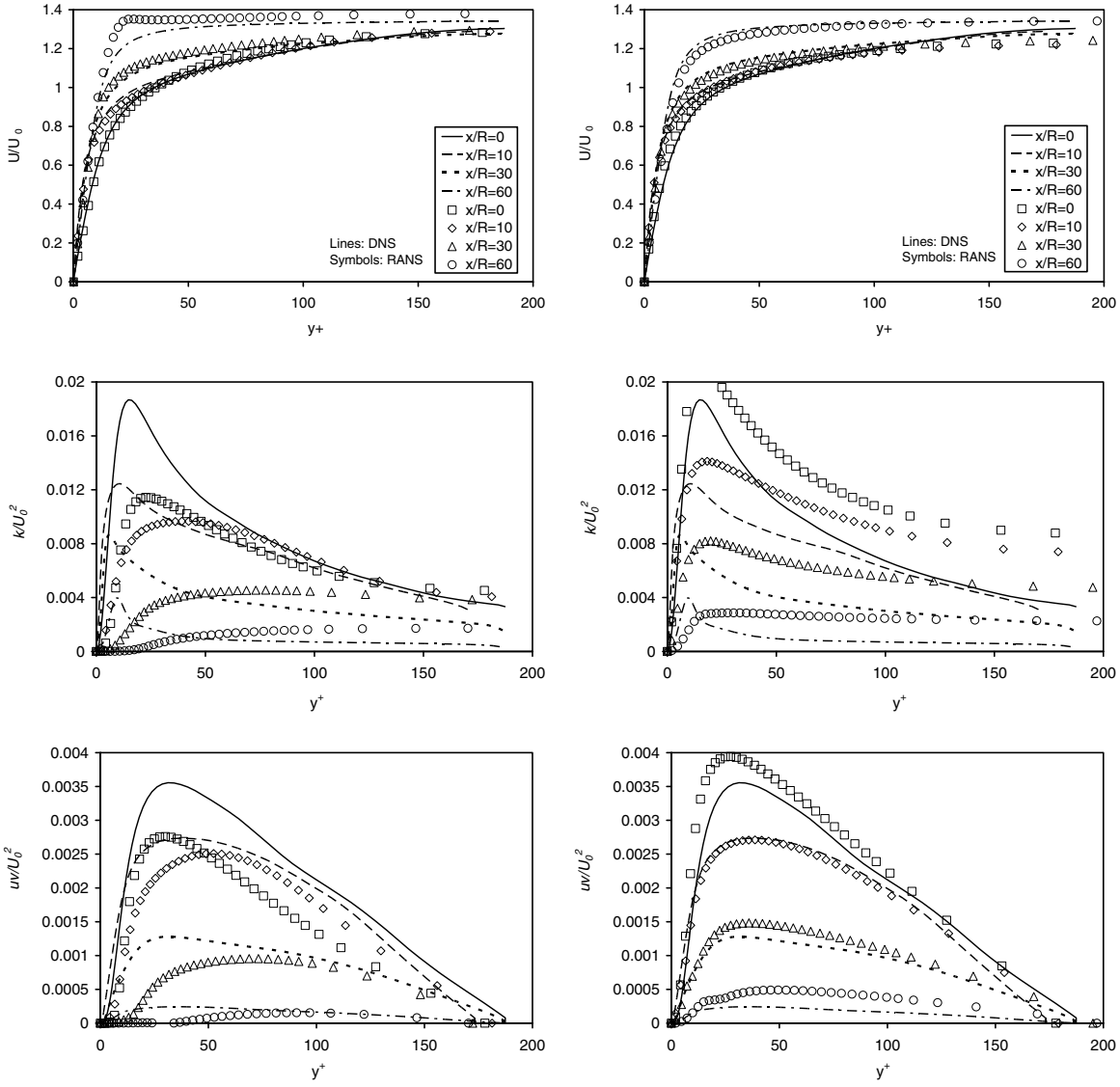

(a) Launder Sharma (LS) Model (b) V2F Model

Fig. 4. Mixed convection with strong flow re-laminarization (Case B).

monotonically along the flow. Even at the end of the pipe, the value of the damping function actually increases dramatically away from the wall region ($y^+ > 40$). The damping function of the LS model reduces significantly near the wall at $x/R = 30$. By the end of the heated flow ($x/R = 60$), the function remains close to zero up to $y^+ = 20$. It is interesting to note though, that turbulent shear stress predicted by the LS model remains close to zero for a much greater distance from the wall (up to $y^+ = 50$). A closer inspection of the results suggests that this is due to the very flat distribution of the velocity profile, leading to a much reduced value of $\widetilde{uv}$. This will be discussed further in the following sub-section. On the other hand, the development of the damping function f_μ of the V2F model follows closely the DNS results, being consistent with the performance of this model shown above. The only exception is the absence of the very large values in the core region at the end of the pipe exhibited by the DNS, but this appears to have little effect on the overall performance of the model. For Group II models, the damping function remains little changed along the pipe of the heated flow since f_μ is a function of y^+ or other variables which do not change with the distortion of the local flow (see Kim et al. [35]). Interestingly, this no-change behaviour appears to have a similar effect to the non-monotonic behaviour of the f_μ of DNS described above, predicting a turbulence distribution reasonably close to that of the DNS.

In the study of air flow reported in Kim et al. [35], it was found important that the damping function of the turbulence model was able to respond to local flows. Group I models were found to perform significantly better than Group II models which was then associated with the ability of the damping functions of the latter group being responsive to local flows. Although at first sight the current results

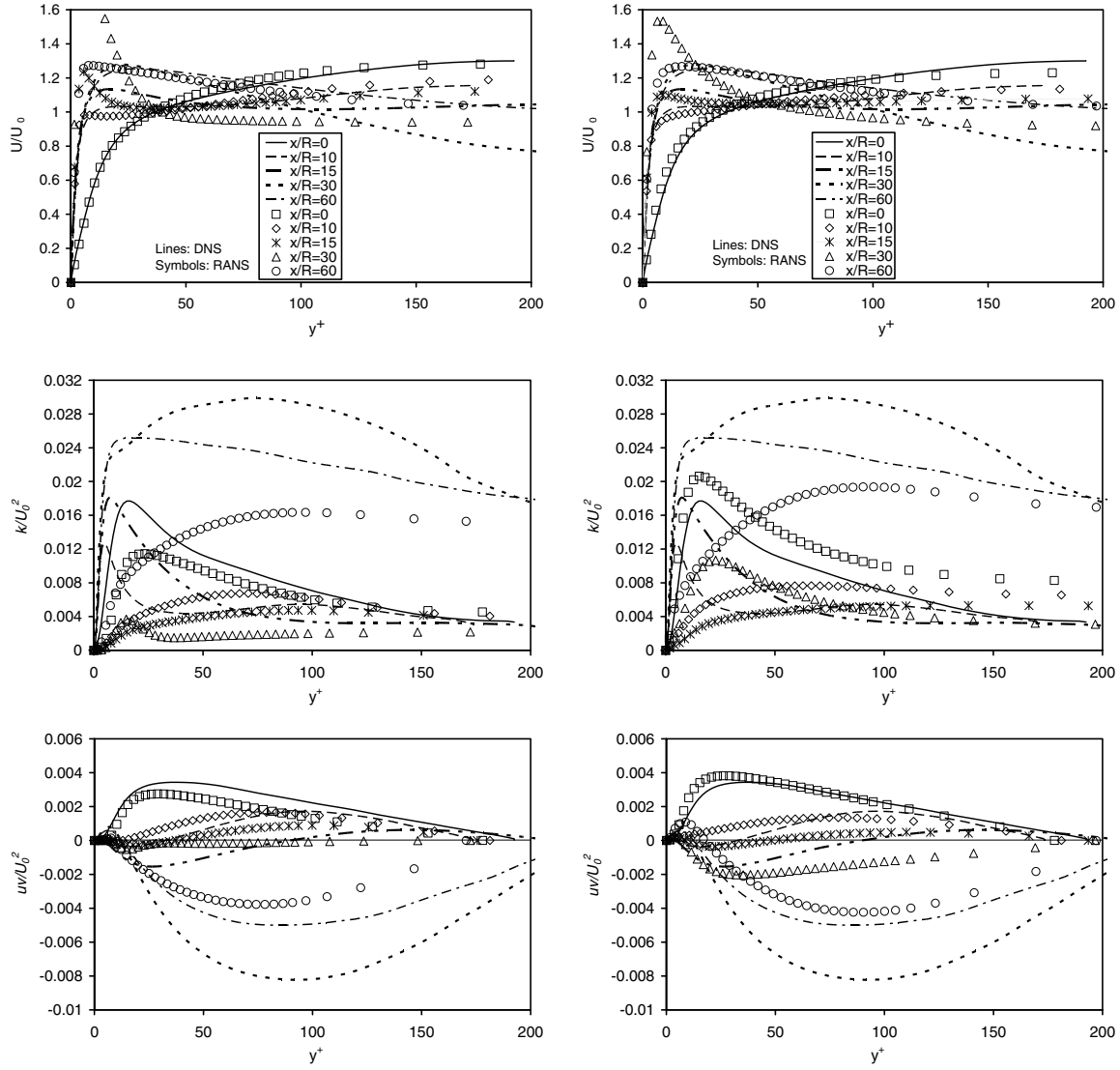

(a) Launder Sharma (LS) Model (b) V2F Model

Fig. 5. Mixed convection in the recovery regime (Case D).

appear to contradict the above conclusions with Group I models now producing less satisfactory results, this is actually not difficult to explain: (i) the general trend of the performance of the turbulence models shown in the two studies is actually quite consistent. In both the current study and that reported in [35], Group I models always respond to the flow distortion more strongly than Group II models do. The reason for the less satisfactory performance of Group I models in the current study is that they *over-respond* to flow distortions and dampened turbulence too soon and too strongly. Although being slow in responding to buoyancy effect under conditions considered in Kim at el. [35], Group II models on the other hand produce better results under the current conditions when both acceleration and buoyancy effects co-exist. This is expected to be caused by some cancelling effects. (ii) On the other hand, the conditions of the flows in the two studies are so different some changes in the performance of the turbulence models are understandable. Firstly, the Boussinesq simplification was used in [35] and therefore the flow acceleration due to heating was absent. The results shown here for Case A suggest that Group I models (including LS) over-laminarize the flow and cause strong heat transfer deterioration in response to the influence of thermally induced flow acceleration. The damping function of Group I models reduces significantly near the wall although that exhibited by the DNS showing a slight increase initially followed by a reduction back to its original value. Clearly such a defect of Group I models did not show in Kim et al. [35]. Secondly, the flow simulated in Kim et al. was at atmospheric pressure and the working fluid (air) was assumed to follow the ideal gas law. The variation of fluid properties with temperature in a flow at a supercritical pressure, such as in the present study, is significantly differ-

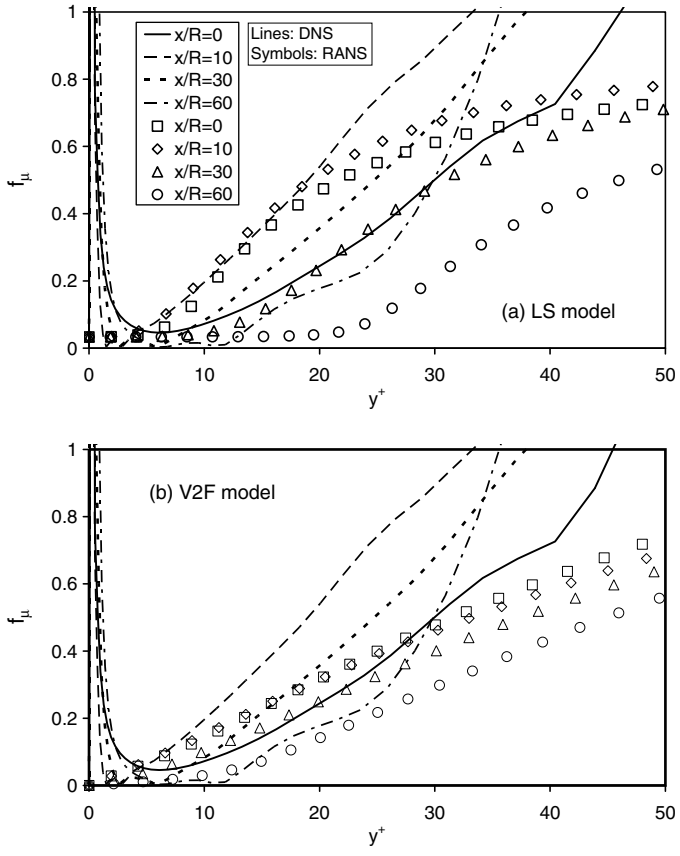

Fig. 6. The damping function (f_μ) in Case B.

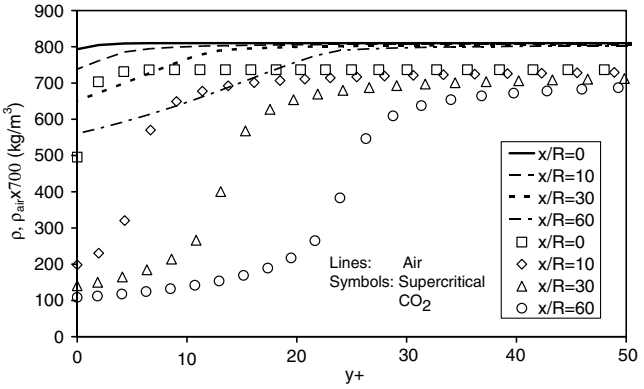

Fig. 7. Radial profiles of density in Case B based on LS model simulation (density for air, ρ_{air}, was computed using the temperature distribution assuming ideal gas at atmosphere).

ent from the ideal gas law, leading to a much different distribution of buoyancy force. Fig. 7 shows the distribution of the density in Case B compared with density distribution calculated using the ideal gas law. The difference is obvious: in the case of supercritical pressure fluid, there appears to be an annular region of light fluid next to the wall (up to $y^+ = 20$ at $x/D = 60$) and a denser fluid in the core region. The density increases sharply within a thin layer, which is centred at the location where the fluid temperature takes the pseudo-critical value. The density distribution of air is on the other hand a simple one, increasing linearly from a lower value at the wall to that of the bulk within the thermal boundary layer.

3.2.3. Flow laminarization and recovery under strong influence of buoyancy (Case D)

In the strongly buoyancy-influenced flow (Case D), the DNS shows that the mean velocity profile is quickly flattened soon after the start of heating, followed by further distortions downstream becoming an inverted M-shaped distribution (Fig. 5). Turbulence production reduces initially ($x/R = 10$), but as the velocity turns into an M-shape, negative shear stress is produced in the core of the pipe and turbulent kinetic energy increases again.

Both the LS and V2F models reproduce the overall trend of flow re-laminarization and recovery, yet their detailed predictions differ significantly from the DNS results. An interesting observation in the DNS is that turbulence has never completely diminished as the flow approaches 'laminarization', noting for example the changes between $x/R = 10$ and 15: (i) negative $\widetilde{uv}$ is generated near the wall well before $\widetilde{uv}$ is completely dampened out in the core and (ii) turbulent kinetic energy remains at a significant level throughout the period of the 'so-called' flow laminarization, particularly near the wall. Both LS and V2F models however predict a much stronger flow laminarization with very low $\widetilde{uv}$ at some stage of the flow, although the V2F model does so to a lesser extent. The strong recovery of turbulent kinetic energy downstream exhibited by the DNS is significantly under-predicted by both models. This contributes to the failure of these turbulence models (and other models tested) in successfully reproducing the strong recovery of heat transfer in strongly buoyancy-influenced flows (Cases C and D).

An important feature of strongly buoyancy-influenced flows is that the velocity profile takes an inverted M-shape with the maximum velocity moving away from the centre of the pipe to a location close to the wall, resulting in a low (including zero) velocity gradient zone. For eddy viscosity turbulence models, this leads to a zone of very low turbulent shear stress. A closer inspection of the DNS results however shows that the locations of the zero-velocity gradient and zero turbulent shear do not coincide. The former is often over some 10 wall units further away from the wall and the value of $\widetilde{uv}$ in the low/zero velocity gradient region can in fact be very big. The eddy viscosity models are clearly intrinsically incapable of predicting this effect.

It is interesting to note that as the buoyancy becomes extremely strong, such as towards the end of the heated flow in Case D, both LS and V2F begin to produce very good predictions of $\widetilde{uv}$, but still significantly low turbulent kinetic energy in comparison with the DNS results, especially near the wall.

Bae et al. [23] commented that, in flows involving a fluid at supercritical pressure, the axial turbulent heat flux $\overline{\rho u'' h''}$

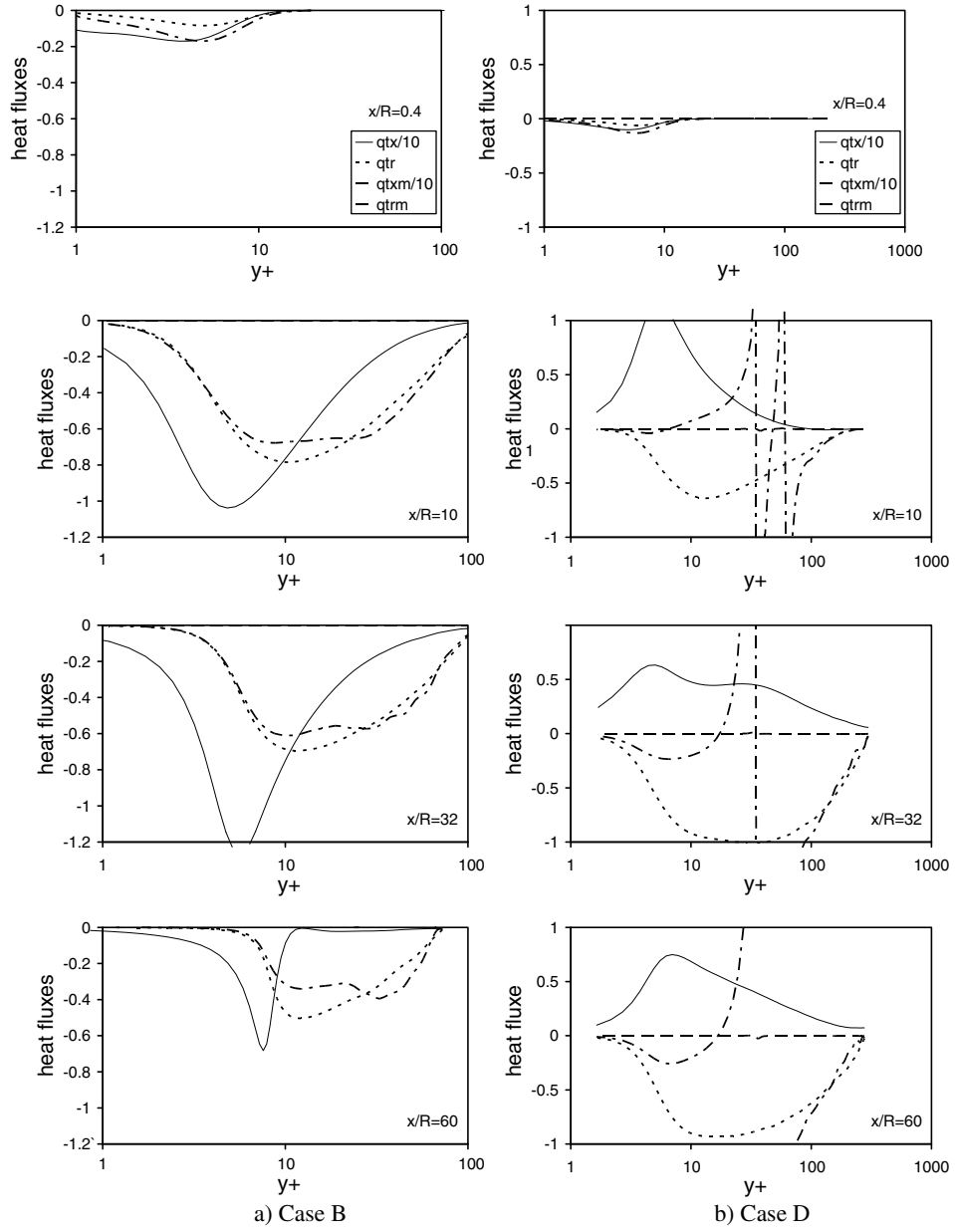

Fig. 8. Turbulent heat fluxes (solid line: $qtx = \overline{\rho u'' h''}/q_w$, dotted line: $qtr = \overline{\rho v'' h''}/q_w$, dash line: $qtxm = \frac{\bar{\mu}_t}{\sigma_T}\frac{\partial \tilde{h}}{\partial x}\frac{1}{q_w}$, chain-dotted line: $qtrm = \frac{\bar{\mu}_t}{\sigma_T}\frac{\partial \tilde{h}}{\partial y}\frac{1}{q_w}$, all based on DNS results).

can be significantly greater than the radial flux $\overline{\rho v'' h''}$ and that the direction of the axial flux can be opposite to the local temperature gradient, both of which will pose a challenge to turbulence modelling. Fig. 8 shows the radial profiles of the axial and radial fluxes obtained from DNS for several axial locations along the heated pipe in Cases B and D. It is clear that (i) the axial flux is always an order of magnitude greater than the radial flux (Note that $\overline{\rho u'' h''}$ has been scaled down 10 times to ensure all of the curves in the figure to be legible); (ii) the axial flux is always negative in Case B whereas it is positive for most part of the heated section in Case D. It should be noted however that turbulent heat flux appears in the energy transport equation in the form of gradient, that is,

$$\frac{\partial(\overline{\rho u'' h''})}{\partial x} \quad \text{and} \quad \frac{\partial(\overline{\rho v'' h''})}{\partial y} \tag{14}$$

Physically, this means that the contribution of the flux to the energy balance of any finite element of fluid in the flow is the difference between the incoming and out-going fluxes from the two opposite surfaces. The larger the gradient the greater the difference. Such 'gradients' are shown in Fig. 9. It is clear that except at the very beginning of the heated flow, the contribution of the axial flux is insignificant in comparison to that of the radial flux. This is due to the fact that the radial temperature gradient in the thermal boundary layer is many times greater than the axial temperature

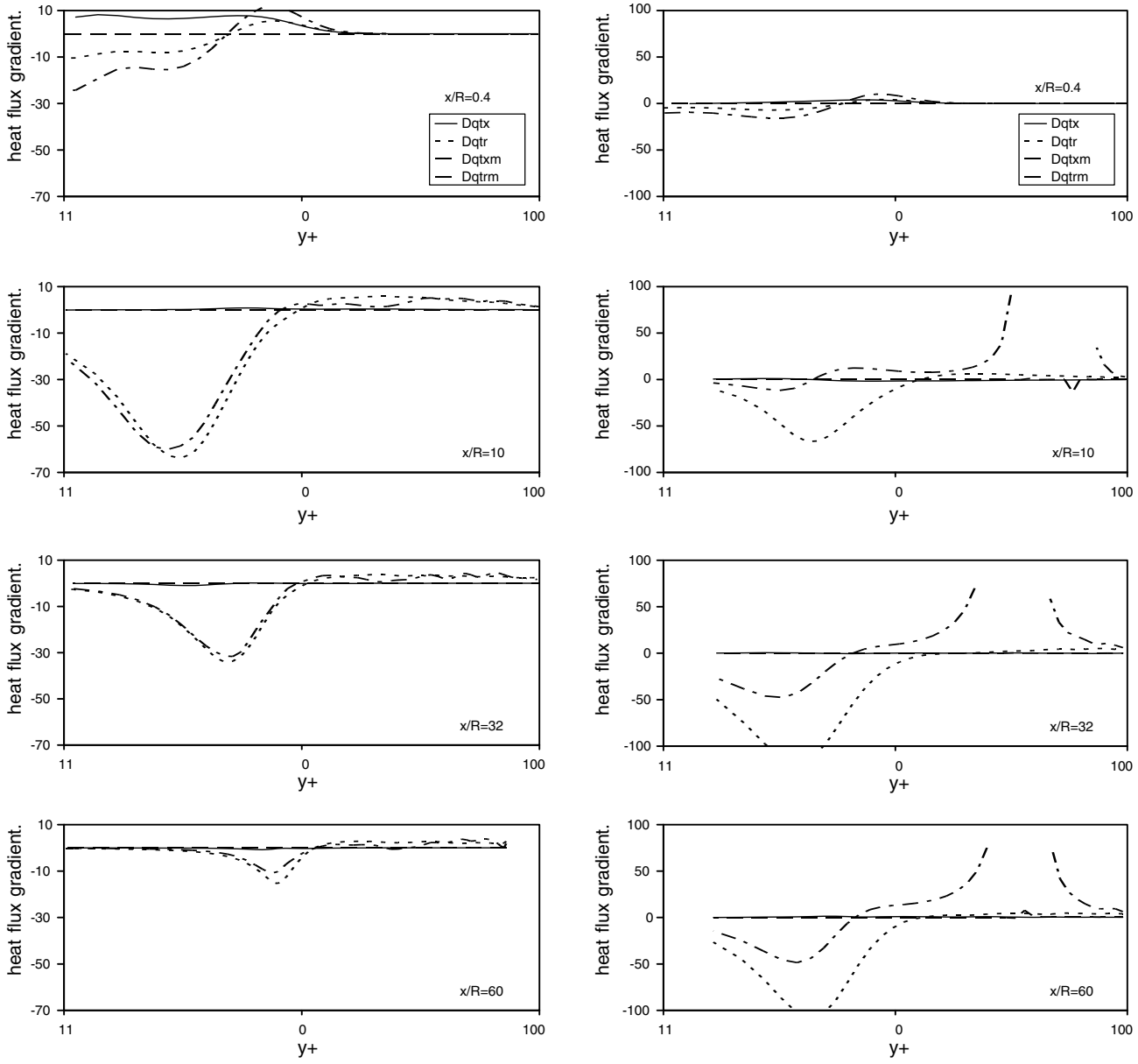

Fig. 9. Turbulent heat flux gradients (solid line: $Dqtx = \frac{\partial(\overline{\rho u'' h''})}{\partial x}\frac{D}{q_w}$), dotted line: $Dqtr = \frac{\partial(\overline{\rho v'' h''})}{\partial y}\frac{D}{q_w}$, dash line: $Dqtxm = \frac{\partial}{\partial x}\left(\frac{\bar{\mu}_t}{\sigma_T}\frac{\partial \tilde{h}}{\partial x}\right)\frac{D}{q_w}$, chain-dotted line: $Dqtrm = \frac{\partial}{\partial y}\left(\frac{\bar{\mu}_t}{\sigma_T}\frac{\partial \tilde{h}}{\partial y}\right)\frac{D}{q_w}$, all based on DNS results.

gradient. Consequently, although the axial flux is big, its gradient is actually small.

Next, it is of interest to examine the suitability of the assumption of constant turbulent Prandtl number. For most eddy viscosity models, the transport equations for turbulent heat flux are not solved, instead heat flux is modelled using turbulent viscosity and the mean temperature gradient as follows:

$$\overline{\rho u'' h''} = \frac{\bar{\mu}_t}{\sigma_T}\frac{\partial \tilde{h}}{\partial x} \quad \text{and} \quad \overline{\rho v'' h''} = \frac{\bar{\mu}_t}{\sigma_T}\frac{\partial \tilde{h}}{\partial y} \tag{15}$$

where σ_T is the turbulent Prandtl number which is normally taken as a constant say 0.9. Figs. 8 and 9 discussed above also show the modelled heat flux calculated using the above equation based on DNS data. Here, the turbulent viscosity μ_t was calculated as follows:

$$\bar{\mu}_t = \bar{\rho}\widetilde{uv}/(\partial\tilde{u}/\partial y + \partial\tilde{v}/\partial x) \tag{16}$$

It is clear that Eq. (15) fails completely to model the large axial heat flux shown in Fig. 8. However since the 'gradient' is insignificant in comparison with the radial heat flux as shown in Fig. 9, this defect should not result in large uncertainties in the overall modelling results. For the radial heat flux, the model reproduces turbulent heat flux very well for Case B over most of the heated length except for near the start of heating. For the strong-buoyancy-influ-

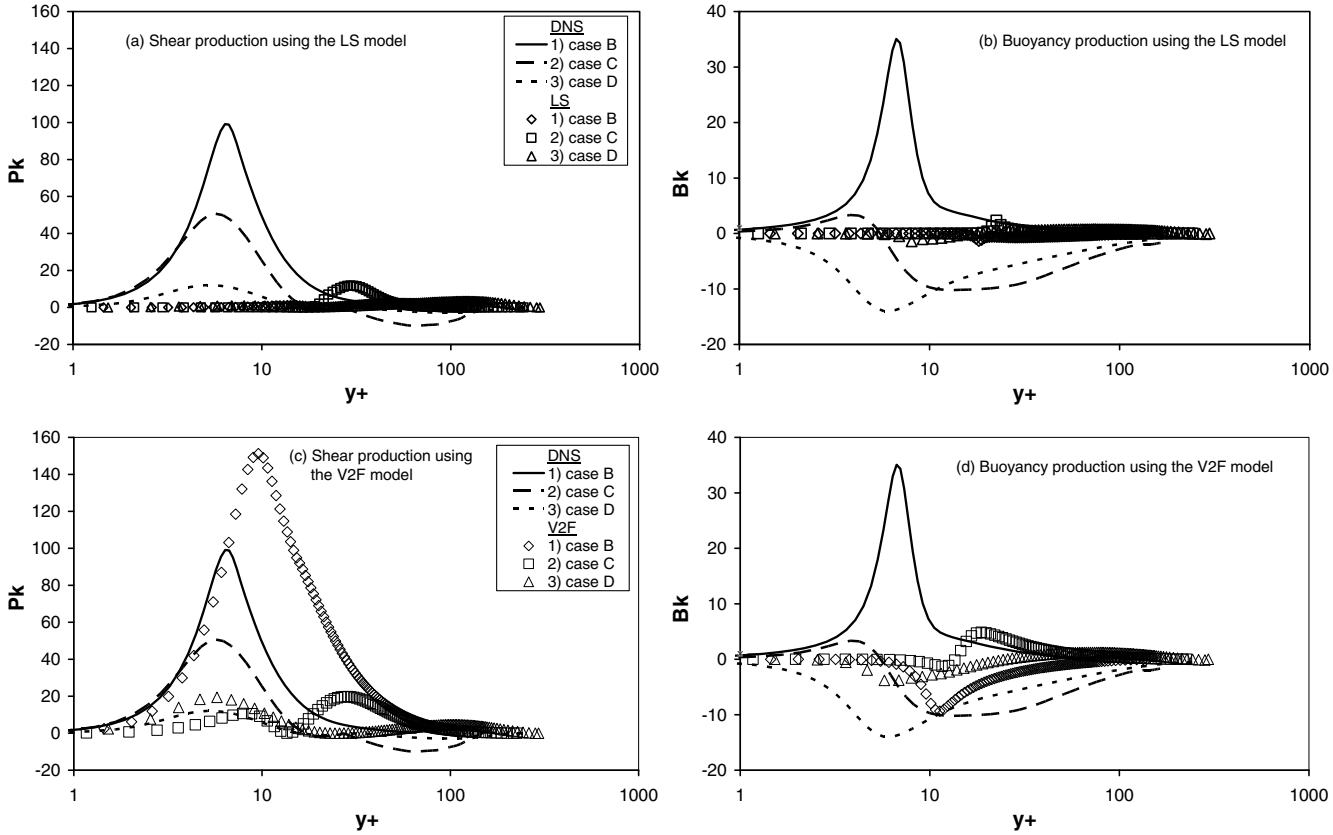

Fig. 10. Production of turbulent kinetic energy due to shear and buoyancy at $x/R = 60$.

enced flows, Case D (and C, not shown here) however, models based on the constant turbulent Prandtl number assumption will have difficulty around the region where the mean velocity gradient is low. As shown in Figs. 8 and 9, the modelled flux and its gradient tend to become unreasonably high there. Even the direction of the flux may be predicted incorrectly in some regions. This is another reason for which the turbulence models tested here are unable to predict the heat transfer recovery in flows where buoyancy is very strong.

3.3. Shear and buoyancy production of turbulence

Fig. 10 shows the shear and buoyancy production of turbulence predicted using the LS and V2F models together with those obtained from DNS. It is useful to summarise the trend exhibited by the DNS data first. The peak shear production is always located around $y^+ = 8$. This is not affected by the inversion of the mean velocity profile (Cases C and D). It is interesting to note that the shear production reduces as the influence of buoyancy increases, from B to C to D, although $\tilde{k}$ gradually increases in these cases, as expected for recovery flows. In the region near the wall, buoyancy production is positive in case B but becomes negative in cases C and D. Taking together the above, the total turbulence production reduces with the increase of buoyancy in the recovery regime although turbulent kinetic energy increases. This can only happen if the dissipation of turbulent kinetic energy ($\tilde{\varepsilon}$) reduces even faster, which is clearly the case. Consequently, in the recovery regime, turbulence is produced and destroyed at a much slower rate even when turbulence is high.

The shear and buoyancy productions predicted by the LS model are much smaller than those obtained from the DNS results. A closer inspection of the results however shows that the trend exhibited by the DNS is more or less reproduced. It is of interest to note that turbulent kinetic energy predicted by the model for Case D is only slightly smaller than that of the DNS although the productions of turbulence are significantly under-predicted by the model. The prediction of the shear production of the V2F model is significantly better than that of the LS model although the comparison with the DNS data is still unsatisfactory. The prediction of the buoyancy production is generally very bad although for the strongest buoyancy-influenced flow (Case D) the general shape of the distribution is closely predicted, showing good potential.

4. Conclusions

The performance of a number of low-Reynolds number turbulence models in predicting heat transfer to carbon dioxide at a supercritical pressure has been assessed by comparing model predictions with DNS. The study has been carried out using an in-house CFD code based on

Favre averaging approach. The main conclusions are as follows:

- Low-Reynolds number turbulence models whose damping functions are based on variables readily responding to buoyancy and flow acceleration (i.e., Group I models, e.g. LS, YS and AKN) significantly over-predict flow laminarization and therefore heat transfer deterioration.
- Turbulence models whose damping functions are based on variables not responding to buoyancy/flow acceleration (i.e., Group II models, e.g. CH and MK) reproduce closely the variations of wall temperature exhibited in the DNS in the forced convection and flow laminarization cases (A and B) although detailed characteristics of the flow and turbulence were not reproduced. The better performance is due to some cancelling effects.
- The V2F model produces the best predictions among all the turbulence models tested.
- Most turbulence models tested reproduce turbulent kinetic energy recovery reasonably well but not the improvement on heat transfer in the strongly buoyancy-influenced cases (C and D). This is partly attributed to the inability of turbulence models in reproducing turbulent heat flux using a constant turbulent Prandtl number. The effect of the lack of a suitable description of axial turbulent heat flux has been shown to be insignificant except at the very beginning of heating.
- The buoyancy production of turbulence is not reproduced by any models tested.

Acknowledgements

The authors gratefully acknowledge the funding for this project provided by UK Engineering and Physical Sciences Research Council (EPSRC) through Grant GR/S19424/02.

Appendix 1. Details of the turbulence models

(A) Constants in the turbulence models

Model	Code	C_μ	$C_{\varepsilon 1}$	$C_{\varepsilon 2}$	σ_k	σ_ε
(1) Abe–Kondoh–Nagano (1994)	AKN	0.09	1.50	1.90	1.4	1.4
(2) Launder–Sharma (1974)	LS	0.09	1.44	1.92	1.0	1.3
(3) Chien (1982)	CH	0.09	1.35	1.80	1.0	1.3
(4) Wilcox (1988)	WI	0.09	1.55	1.83	2.0	2.0
(5) Yang–Shih (1993)	YS	0.09	1.44	1.92	1.0	1.3
(6) Myoung–Kasagi (1990)	MK	0.09	1.40	1.80	1.4	1.3
(7) V2-F (1998)	V2F	0.22	1.4	1.9	1.0	1.3

(B) Functions in the turbulence models

Code	f_μ	f_1	f_2
AKN	$\left[1+\frac{5}{Re_t^{0.75}}\exp\left(-\left(\frac{Re_t}{200}\right)^2\right)\right]\left(1-\exp\left(-\frac{y^*}{14}\right)\right)^2$	1.0	$\left\{1-0.3\exp\left(-\left(\frac{Re_t}{6.5}\right)^2\right)\right\}\left[1-\exp\left(-\frac{y^*}{3.1}\right)\right]^2$
LS	$\exp\left[\frac{-3.4}{(1+Re_t/50)^2}\right]$	1.0	$1-0.3\exp(-Re_t^2)$
CH	$1-\exp(-0.0115y^+)$	1.0	$1-0.22\exp\left(\frac{-Re_t^2}{36}\right)$
WI	1.0	1.0	1.0
YS	$(1+1/\sqrt{Re_t})\left[1-\exp\begin{pmatrix}-1.5\times10^{-4}Re_y\\-5.0\times10^{-7}Re_y^3\\-1.0\times10^{-10}Re_y^5\end{pmatrix}\right]^{0.5}$	$\frac{\sqrt{Re_t}}{1+\sqrt{Re_t}}$	$\frac{\sqrt{Re_t}}{1+\sqrt{Re_t}}$
MK	$[1-\exp(-y^+/70)]\left(1+\frac{3.45}{Re_t^{1/2}}\right)$	1.0	$\left\{1-\frac{2}{9}\exp\left(-\left(\frac{Re_t}{6}\right)^2\right)\right\}\left[1-\exp\left(-\frac{y^+}{5}\right)\right]^2$
V2F	$\frac{\overline{v^2}}{k}$	$1+0.045\sqrt{\frac{k}{\overline{v^2}}}$	1.0

(C) D and E terms and wall boundary conditions for $\tilde{k}$ and $\tilde{\varepsilon}$

Code	D	E	Wall BC
AKN	0	0	$k_w = 0,\ \varepsilon_w = 2\frac{\bar{\mu}}{\bar{\rho}}\frac{\tilde{k}}{y^2}$
LS	$2\frac{\bar{\mu}}{\bar{\rho}}\left(\frac{\partial\sqrt{\tilde{k}}}{\partial y}+\frac{\partial\sqrt{\tilde{k}}}{\partial x}\right)^2$	$2\frac{\bar{\mu}\bar{\mu}_t}{\bar{\rho}\bar{\rho}}\left[\left(\frac{\partial^2\tilde{v}}{\partial x^2}\right)^2+\left(\frac{\partial^2\tilde{u}}{\partial y^2}\right)^2\right]$	$k_w = 0,\ \tilde{\varepsilon}_w = 0$
CH	$2\frac{\bar{\mu}\tilde{k}}{\bar{\rho}}\left(\frac{1}{y^2}\right)$	$\frac{-2\bar{\mu}\tilde{\varepsilon}}{\bar{\rho}y^2}\exp(-0.5y^+)$	$k_w = 0,\ \tilde{\varepsilon}_w = 0$
WI	0	$-2\left(\frac{\bar{\mu}}{\bar{\rho}}+\frac{\bar{\mu}_t}{2\bar{\rho}}\right)\left(\frac{\partial\tilde{k}}{\partial y}+\frac{\partial\tilde{k}}{\partial x}\right)\left[\frac{\partial}{\partial y}\left(\frac{\tilde{\varepsilon}}{\tilde{k}}\right)+\frac{\partial}{\partial x}\left(\frac{\tilde{\varepsilon}}{\tilde{k}}\right)\right]$	$k_w = 0,\ \varepsilon_w = \frac{\bar{\mu}}{\bar{\rho}}\frac{\partial^2\tilde{k}}{\partial y^2}$
YS	0	$2\frac{\bar{\mu}\bar{\mu}_t}{\bar{\rho}\bar{\rho}}\left[\left(\frac{\partial^2\tilde{v}}{\partial x^2}\right)^2+\left(\frac{\partial^2\tilde{u}}{\partial y^2}\right)^2\right]$	$k_w = 0,\ \varepsilon_w = 2\frac{\bar{\mu}}{\bar{\rho}}\left(\frac{\partial\sqrt{\tilde{k}}}{\partial y}\right)^2$
MK	0	0	$k_w = 0,\ \varepsilon_w = \frac{\bar{\mu}}{\bar{\rho}}\frac{\partial^2\tilde{k}}{\partial y^2}$
V2F	0	0	$k_w = 0,\ \varepsilon_w = \frac{\bar{\mu}}{\bar{\rho}}\frac{\partial^2\tilde{k}}{\partial y^2}$
Note	$Re_t = \frac{\bar{\rho}\tilde{k}^2}{\bar{\mu}\tilde{\varepsilon}},\quad Re_y = \frac{y\bar{\rho}\tilde{k}^{1/2}}{\bar{\mu}},\quad y^+ = \frac{\bar{\rho}y}{\bar{\mu}}\sqrt{\tau_w/\bar{\rho}},\quad y^* = \frac{\bar{\rho}y}{\bar{\mu}}u_\varepsilon,\quad u^+ = \frac{\tilde{u}}{\sqrt{\tau_w/\bar{\rho}}},\quad \tau_w = \bar{\mu}\frac{d\tilde{u}}{dy},\quad u_\varepsilon = (\bar{\mu}\tilde{\varepsilon}/\bar{\rho})^{0.25}$		

(1) The Wilcox model equation was converted to an equation for ε.

References

[1] G.R. Dimmick, V. Chatoorgoon, H.F. Khartabil, R.B. Duffey, Natural-convection studies for advanced CANDU reactor concepts, Nucl. Eng. Design 230 (1–3) (2004) 69–91.

[2] S. Koshizuka, Y. Oka, Supercritical pressure, light-water-cooled reactors for economical nuclear power plants, Progr. Nucl. Energy 32 (3/4) (1998) 547–554.

[3] Ning Zhou, Anantha, Krishman, Frederic Vogel, William A. Peters, A computational model for supercritical water oxidation of organic toxic wastes, Adv. Environ. Res. 4 (2000) 79–95.

[4] S.S. Pitla, E.A. Groll, S.R. Ramadhyani, Convective heat transfer in-tube flow of turbulent supercritical carbondioxide, Part 1 – numerical analysis, HVAC&R Res. 7 (4) (2001) 345–366.

[5] S.S. Pitla, E.A. Groll, S.R. Ramadhyani, Convective heat transfer in-tube flow of turbulent supercritical carbondioxide, Part 2 – experimental data and numerical predictions, HVAC&R Res. 7 (4) (2001) 367–382.

[6] B. Youn, A.F. Mills, Flow of supercritical hydrogen in a uniformly heated circular tube, Numer. Heat Transfer Part A v24 (1993) 1–24.

[7] I.L. Pioro, R.B. Duffey, Experimental heat transfer in supercritical water flowing inside channels (survey), Nucl. Eng. Design 235 (2005) 2407–2430.

[8] R.B. Duffey, I.L. Pioro, Experimental heat transfer of supercritical carbon dioxide flowing inside channels (survey), Nucl. Eng. Design 235 (2005) 913–924.

[9] C. Dang, E. Hihara, In-tube cooling heat transfer of supercritical carbon dioxide. Part 1. Experimental measurement, Int. J. Refrigerat. – Revue Int. Du Froid 27 (2004) 736–747.

[10] S.M. Liao, T.S. Zhao, An experimental investigation of convection heat transfer to supercritical carbon dioxide in miniature tubes, Int. J. Heat Mass Transfer 45 (2002) 5025–5034.

[11] S.M. Liao, T.S. Zhao, Measurements of heat transfer coefficients from supercritical carbon dioxide flowing in horizontal mini/micro-channels, ASME J. Heat Transfer 124 (2) (2002) 413–420.

[12] P.X. Jiang, Y.J. Xu, J. Lv, R.F. Shi, S. He, J.D. Jackson, Experimental investigation of convection heat transfer of CO_2 at super-critical pressures in vertical mini-tubes and in porous media, Appl. Therm. Eng. 24 (2004) 1255–1270.

[13] J.K. Kim, H.K. Jeon, J.S. Lee, Wall temperature measurement and heat transfer correlation of turbulent supercritical carbon dioxide flow in vertical circular/non-circular tubes, Nucl. Eng. Design 237 (2007) 1795–1802.

[14] C.B. Dang, E. Hihara, In-tube cooling heat transfer of supercritical carbon dioxide. Part 2. Comparison of numerical calculation with different turbulence models, Int. J. Refrigerat.– Revue Int. Du Froid 27 (2004) 748–760.

[15] S. Koshizuka, N. Takano, Y. Oka, Numerical-analysis of deterioration phenomena in heat-transfer to supercritical water, Int. J. Heat Mass Transfer 38 (1995) 3077–3084.

[16] S. He, W.S. Kim, P.X. Jiang, J.D. Jackson, Simulation of mixed convection heat transfer to carbon dioxide at supercritical pressure, Proc. Institut. Mechan. Eng. Part C – J. Mechan. Eng. Sci. 218 (2004) 1281–1296.

[17] S. He, P.X. Jiang, Y.J. Xu, R.F. Shi, W.S. Kim, J.D. Jackson, A computational study of convection heat transfer to CO_2 at supercritical pressures in a vertical mini tube, Int. J. Therm. Sci. 44 (2005) 521–530.

[18] S.H. Lee, J.R. Howell, Turbulent developing convective heat transfer in a tube for fluids near the critical point, Int. J. Heat Mass Transfer 41 (1998) 1205–1218.

[19] P. Asinari, Numerical prediction of turbulent convective heat transfer in mini/micro-channels for carbon dioxide at supercritical pressure, Int. J. Heat Mass Transfer 48 (2005) 3864–3879.

[20] M.B. Sharabi, W. Ambrosini, S. He, Prediction of unstable behaviour in a heated channel with water at supercritical pressure by CFD models, Ann. Nucl. Energy 35 (2008) 767–782.

[21] J. Yang, Y. Oka, Y. Ishiwatari, J. Liu, J. Yoo, Numerical investigation of heat transfer in upward flows of supercritical water in circular tubes and tight fuel rod bundles, Nucl. Eng. Design 237 (2007) 420–430.

[22] X. Cheng, B. Kuang, Y.H. Yang, Numerical analysis of heat transfer in supercritical water cooled flow channels, Nucl. Eng. Design 237 (2007) 240–252.

[23] J.H. Bae, J.Y. Yoo, H. Choi, Direct numerical simulation of turbulent supercritical flows with heat transfer, Phys. Fluids 17 (2005) 1–24.

[24] PROPATH Group, PROPATH: A Program Package for Thermophysical Properties of Fluids, Ver. 11.1. The International Association for the Properties of Water and Steam (IAPWS). <http://www.iapws.org>, 1999.

[25] A.M. Shehata, D.M. McEligot, Mean turbulence structure in the viscous layer of strongly heated internal gas flows, Measure. Int. J. Heat Mass Transfer 41 (1998) 4297.

[26] B.E. Launder, B.L. Sharma, Application of the energy-dissipation of turbulence to calculation of low near a spinning disc, Lett. Heat Mass Transfer 1 (1974) 131–138.

[27] K.Y. Chien, Predictions of channel and boundary-layer flows with a low-Reynolds number turbulence model, AIAA J. 20 (1982) 33–38.
[28] D.C. Wilcox, Reassessment of the scale determining equation for advanced turbulence models, AIAA J. 26 (1988) 1299–1310.
[29] H.K. Myoung, N. Kasagi, A new approach to the improvement of k-ε turbulence model for wall bounded shear flows, JSME Int. J. 33 (1990) 63–72.
[30] Z. Yang, T.H. Shih, New time scale based k-ε model for near-wall turbulence, AIAA J. 31 (1993) 1191–1198.
[31] K. Abe, T. Kondoh, Y. Nagano, A new turbulence model for predicting fluid flow and heat transfer in separating and reattaching flow, Int. J. Heat Mass Transfer 37 (1994) 139–151.
[32] M. Behnia, S. Parneix, P.A. Durbin, Prediction of heat transfer in an axisymmetric turbulent jet impinging on a flat plate, Int. J. Heat Mass Transfer 41 (1998) 1845–1855.
[33] J. Fewster, J.D. Jackson, Some experiments on heat transfer to carbon dioxide at supercritical pressure in tubes, in: Proceedings of the International Congress on Advances in Nuclear Power Plants (ICAPP'04), Pittsburg, PA USA, 13th–17th June, 2004.
[34] S. He, W.S. Kim, J.D. Jackson, A computational study of convective heat transfer to carbon dioxide at a pressure just above the critical value, Appl. Therm. Eng. (2007), doi:10.1016/j.applthermaleng.2007.11.001.
[35] W.S. Kim, S. He, J.D. Jackson, Assessment of predictions of turbulence models of mixed convection by comparison with DNS, Int. J. Heat Mass Transfer 51 (2008) 1293–1312.